1    **Structural insight into *Pichia pastoris* fatty acid synthase**

2

3    Joseph S. Snowden, Jehad Alzahrani, Lee Sherry, Martin Stacey, David J. Rowlands,

4    Neil A. Ranson* & Nicola J. Stonehouse*+

5

6    Astbury Centre for Structural Molecular Biology, School of Molecular & Cellular

7    Biology, Faculty of Biological Sciences, University of Leeds, Leeds, LS2 9JT, UK.

8

9    *Corresponding authors: n.a.ranson@leeds.ac.uk, n.j.stonehouse@leeds.ac.uk

10

11    + Lead contact

12

13    <u>**Summary**</u>

14    Type I fatty acid synthases (FASs) are critical metabolic enzymes which are common

15    targets for bioengineering in the production of biofuels and other products.

16    Serendipitously, we identified FAS as a contaminant in a cryoEM dataset of virus-like

17    particles (VLPs) purified from *P. pastoris*, an important model organism and common

18    expression system used in protein production. From these data, we determined the

19    structure of *P. pastoris* FAS to 3.1 Å resolution. While the overall organisation of the

20    complex was typical of type I FASs, we identified several differences in both structural

21    and enzymatic domains through comparison with the prototypical yeast FAS from *S.*

22    *cerevisiae*. Using focussed classification, we were also able to resolve and model the

23    mobile acyl-carrier protein (ACP) domain, which is key for function. Ultimately, the

24    structure reported here will be a useful resource for further efforts to engineer yeast

25    FAS for synthesis of alternate products.

26

27    Keywords: CryoEM - cryo-electron microscopy, FAS – fatty acid synthase, VLP –

28    virus-like particle

29

## Introduction

31 Fatty acid synthases (FASs) are critical metabolic enzymes for the endogenous

32 biosynthesis of fatty acids in a diverse range of organisms. Through iterative cycles of

33 chain elongation, FASs catalyse the synthesis of long-chain fatty acids that can

34 produce raw materials for membrane bilayer synthesis, lipid anchors of peripheral

35 membrane proteins, metabolic energy stores, or precursors for various fatty acid-

36 derived signalling compounds[1]. In addition to their key physiological importance,

37 microbial FAS systems are also a common target of metabolic engineering

38 approaches, usually with the aim of generating short chain fatty acids for an expanded

39 repertoire of fatty acid-derived chemicals, including chemicals with key industrial

40 significance such as $\alpha$-olefins[2–5]. A comprehensive structural and functional

41 understanding of a diverse range of FAS systems is therefore paramount to the

42 success of such complex rational engineering approaches.

43

44 Unlike the dissociated systems of individual enzymes that make up type II FAS

45 systems in plants and bacteria[6], Type I FAS systems in fungi and animals are large

46 complexes that integrate the key enzymes required for fatty acid biosynthesis[7,8]. In

47 particular, yeast type I FASs are 2.6 MDa hetero-dodecameric complexes with an $\alpha_6\beta_6$

48 configuration, which form a cage-like structure comprising two dome-shaped reaction

49 chambers on either side of a central platform[9–13]. Along with structural support regions,

50 enzymatic domains form the walls of the reaction chambers, with most active sites

51 facing the chamber interior. The mobile acyl-carrier protein (ACP) domain tethers the

52 growing fatty acid chain and carries it between active sites, so each can act on this in

53 turn[13,14]. The phosphopantetheine transferase (PPT) domain, which catalyses the

54 attachment of a phosphopantetheinyl group to the active site serine residue of the

55 ACP (necessary for ACP activity), is also an integral part of yeast FAS complexes,

56 and is located on the exterior of the cage[12,15].

57

58 A deep body of work underlies our current structural understanding of yeast FAS,

59 although FAS structure determination to date has been challenging. A cryoEM study

60 of *S. cerevisiae* FAS revealed a number of differences with X-ray crystal structures of

61 fungal FASs, suggesting that crystal contacts had altered the conformation of FAS

62 from its unconstrained structure in solution[13]. A more recent attempt to determine the

2

63  solution structure of *S. cerevisiae* FAS at a resolution sufficient for molecular modelling
64  was hindered by partial denaturation induced by interactions with the air-water
65  interface, an effect that was ameliorated by coating grids with hydrophilized graphene,
66  ultimately leading to a 3.1-Å resolution structure when sample preparation was
67  optimised[16,17].

68

69  While our understanding of yeast FAS structure is growing, our library of structures
70  remains incomplete. The vast majority of published solution structures of FAS are from
71  *S. cerevisiae*[13,16–19]. To date, no structures are available for *Pichia pastoris* FAS from
72  either cryoEM or X-ray crystallography. *P. pastoris* (*Komagataella spp.*) is a
73  methylotrophic yeast which is used extensively for recombinant protein production[20].
74  In recent years, it has also been the target of metabolic engineering approaches[21]. *P.*
75  *pastoris* has a major advantage over other yeast strains like *S. cerevisiae*, as it
76  produces relatively little ethanol, making the maintenance of productive, high-cell
77  density fermenter cultures more tractable[22]. It has also been suggested that *P. pastoris*
78  cells, in contrast to cells of the plant *Arabidopsis* sp., are highly tolerant of free fatty
79  acids[23].

80

81  Here, we report the 3.1-Å resolution solution structure of *P. pastoris* FAS, determined
82  by cryoEM. We initially identified FAS as a contaminant in a *P. pastoris*-derived virus-
83  like particle (VLP) preparation being used for structural studies, and processed these
84  data to yield detailed structural information on FAS, including density for the mobile
85  ACP domain. Comparison of our atomic model with that of *S. cerevisiae* revealed
86  interesting structural differences throughout the complex within both structural and
87  enzymatic domains. This included movement of the malonyl/palmitoyl transferase
88  domain at the level of domain packing, and alternative rotamers in the catalytic centres
89  of the acyl transferase and enoylreductase domains.

90

91  **Results**

92

93  **CryoEM structure determination of *Pichia pastoris* fatty acid synthase**
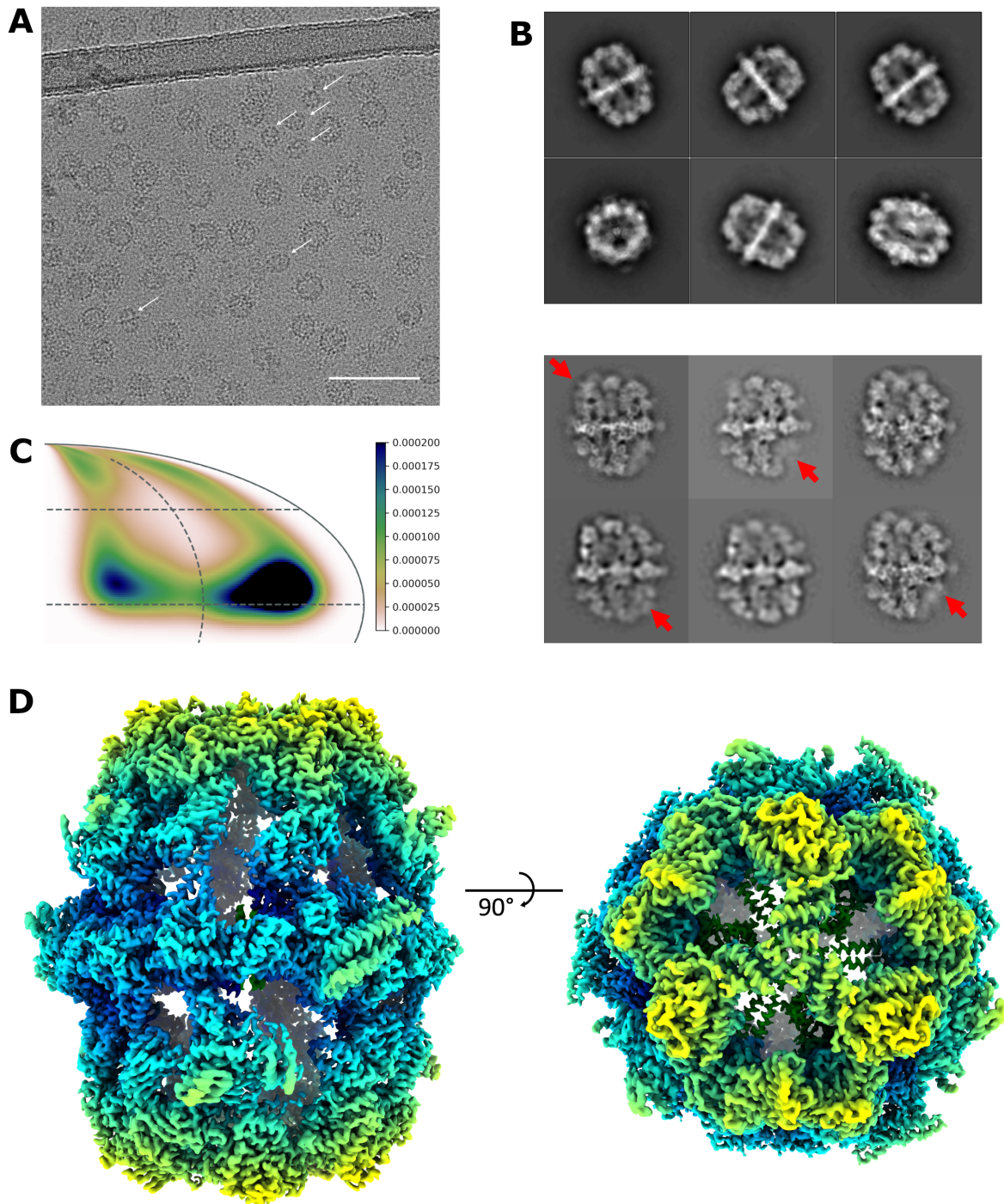94  Virus-like particles (VLPs) composed of hepatitis B virus tandem core proteins[24] with
95  a SUMO-binding affimer inserted into the major immunodominant region (MIR)[25] were
96  expressed in transformed *P. pastoris* cells for structural and vaccine studies (construct

97    available upon request). Expression was induced with methanol and the VLPs purified

98    from the yeast lysate by sucrose gradient centrifugation. Image analysis of cryoEM

99    data revealed, in addition to the VLPs, non-VLP-like particles which were recognised

100   as yeast FAS complexes due to their characteristic morphology – two hollow chambers

101   on either side of a central platform. Further inspection of individual micrographs

102   revealed that FAS particles were well-separated from VLPs, indicating that FAS was

103   not co-purified as a result of an association with the VLPs (Fig 1A).

104

105   In contrast to a recent study that reported significant air-water interface-induced

106   denaturation of FAS particles by cryoEM (which could be solved with deposition of

107   hydrophilized graphene on the grid surface)[16], we saw no signs of denaturation in our

108   data set, judged by 2D class averages (Fig 1B). While some particles were discarded

109   after the initial 2D classification, ~67% of these were actually VLPs or areas of carbon

110   film that were inadvertently selected during autopicking, and the remaining discarded

111   classes mainly comprised apparently intact FAS particles over thick carbon. It is

112   therefore difficult to estimate how many particles were excluded because of damage

113   that was not visible in class averages. There was evidence of some preferential

114   orientation effects (perhaps induced by adsorption to the carbon film), but this was not

115   a significant problem, as a reasonable coverage of potential orientations within the

116   asymmetric unit of the D3 symmetric structure (i.e., a single $\alpha$ and $\beta$ subunit) was

117   achieved (Fig 1C).

118

119   Classes corresponding to FAS were taken forward and processed separately, yielding

120   a 3.1 Å reconstruction from ~37,000 particles, with parts of the central platform

121   resolved to ~2.7 Å (Fig 1D, Supplementary Fig S1). In comparison, ~28,000 particles

122   of *S. cerevisiae* FAS were used to generate a 4.0-Å resolution structure[16]. More

123   recently, ~15,000 particles of *S. cerevisiae* FAS led to a 3.1-Å resolution map,

124   although in this case the FAS was incubated with NADPH and malonyl-CoA before

125   vitrification in order to drive synthesis of fatty acids to completion, increasing particle

126   homogeneity[17].

127



*Figure 1. Determination of P. pastoris FAS structure by cryoEM. (A) Raw micrograph showing VLPs with contaminating FAS particles. FAS particles are indicated by white arrows. Scale bar shows 100 nm. (B) The most populated classes from 2D classification of P. pastoris FAS (after excluding 'junk' classes of FAS over thick carbon support) (upper) compared with 2D class averages of S. cerevisiae FAS showing partial denaturation (indicated by red arrows) from D'Imprima et al. (2019)[16]*

134 *(licensed under CC BY 4.0) (lower). **(C)** Orientation distribution map of particles*

135 *contributing to the final reconstruction of the FAS asymmetric unit. The map shows*

136 *the probability that any particle was assigned the orientation indicated, according to*

137 *the scale shown. **(D)** CryoEM density map of P. pastoris FAS, coloured radially.*

138

**139 The 3.1-Å resolution solution structure of *P. pastoris* FAS**

140 The overall structure of the *P. pastoris* FAS reported here was typical of a yeast FAS.

141 Density was present for most domains of the $\alpha$- and $\beta$-subunits, including acyl

142 transferase (AT), ketoacyl reductase (KR), ketoacyl synthase (KS), enoylreductase

143 (ER), dehydratase (DH) and malonyl/palmitoyl transferase (MPT) domains (Fig 2A,B).

144 ACP density was weak (only becoming fully apparent when inspecting the map at a

145 threshold of approx. 1 $\sigma$) and poorly resolved, as was also the case for previous EM

146 density maps of *S. cerevisiae* FAS (e.g., EMD-10420, EMD-0178). However, the

147 approximate position of the ACP could be identified within the reaction chamber. There

148 was no density apparent for the PPT region, as discussed further below.

149

150 The map was sufficiently resolved to allow us to build an atomic model of *P. pastoris*

151 FAS. An initial homology model for the asymmetric unit was generated using SWISS-

152 MODEL[26] and rigid-body fitted into the density map. The fit of model to density was

153 visually inspected and corrected, before the model was symmetrised and refined to

154 improve its fit to the density and geometry. The $\alpha$ subunit is mostly resolved, though

155 several segments of the peptide sequence (including the ACP and PPT domains) are

156 missing (residues 96-322, 535-598 and 1752-1879). The $\beta$ subunit is practically

157 complete, lacking only a small number of residues at the N- and C-termini (residues

158 1-9 and 2064-2069). We also observed density for a ligand bound within the active

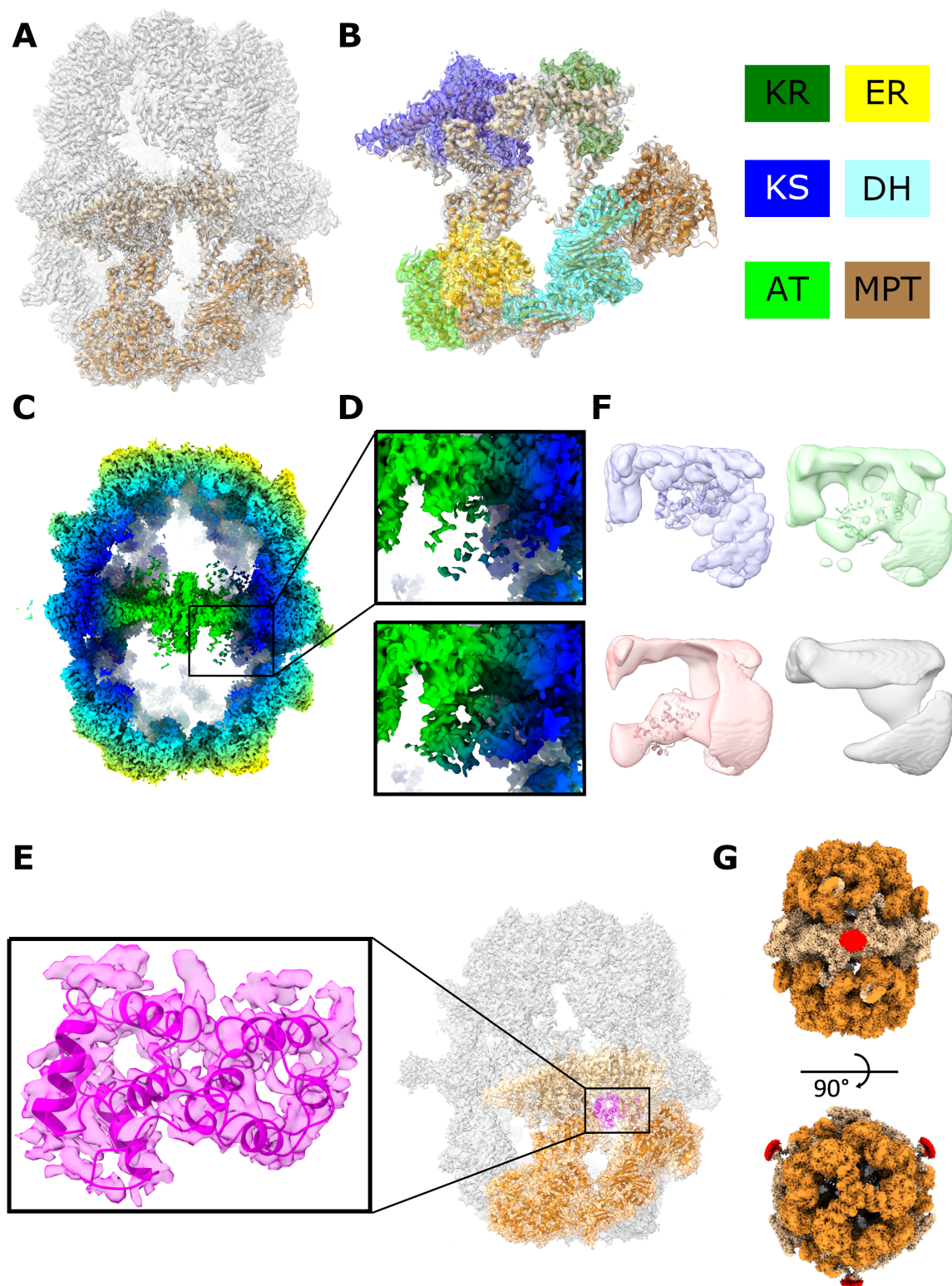159 site of the ER domain (for reference, see Fig 3G), presumably a molecule of FMN.

160

**Figure 2. The molecular structure of P. pastoris FAS. (A)** *Atomic coordinates for the asymmetric unit of P. pastoris FAS, comprising $\alpha$ (light orange) and $\beta$ (dark orange) subunits, with the density map overlaid. **(B)** Enlarged view of the asymmetric unit, highlighting different enzymatic domains according to the colour scheme indicated.*

166    *Grey-coloured regions are non-enzymatic, structural domains. Domain boundaries*
167    *were assigned based on equivalent domain boundaries from S. cerevisiae FAS. KR –*
168    *ketoacyl reductase, KS – ketoacyl synthase, AT – acetyl transferase, ER –*
169    *enoylreductase, DH – dehydratase, MPT – malonyl/palmitoyl transferase. **(C)** Clipped*
170    *view of the sharpened FAS density map, coloured according to radius. The box*
171    *highlights the region of the reaction chamber selected for the first focussed 3D*
172    *classification. **(D)** Enlarged image of the region depicted by the box in (C) (upper)*
173    *compared with the sharpened, asymmetric reconstruction of FAS derived from an ACP*
174    *density-containing class from the first focussed 3D classification (lower). All classes*
175    *from the first focussed classification are given in Supplementary Fig S2A. **(E)** Atomic*
176    *coordinates for the ACP domain of FAS fitted into ACP density from the map shown*
177    *in (D, bottom). ACP is also shown in the context of the full FAS complex. **(F)***
178    *Representative classes from the second focussed 3D classification (with expanded*
179    *masked region) of the complex interior. Atomic coordinates for ACP are shown fitted*
180    *into the three classes containing putative ACP density to give an indication of size.*
181    *One class shows no putative density for ACP (lower right). All maps are shown at the*
182    *same contour level. All classes from the second focussed classification are given in*
183    *Supplementary Fig S2B. **(G)** Density map of FAS shown at a low contour level (i.e.,*
184    *including weak density), coloured according to subunit ($\alpha$ - light orange, $\beta$ - dark*
185    *orange). Unexplained density, not accounted for by FAS subunits $\alpha$ or $\beta$, is highlighted*
186    *in red.*

187

188    In an attempt to improve the quality of the cryoEM density corresponding to the ACP
189    domain, we performed focussed 3D classification within the reaction chamber of the
190    complex (Fig 2C). While classification with a regularisation parameter ('T' number) of
191    20 did not reveal any meaningful classes, using a higher value of 40 (i.e., putting a
192    higher relative weighting on the experimental data than on the prior/reference) yielded
193    a class containing relatively well resolved ACP density (Supplementary Fig S2A).
194    Particles from this class were taken forward for asymmetric reconstruction, yielding a
195    complete FAS map of 3.1-Å resolution (Fig 2D). In the latter map, the additional density
196    is consistent with the ACP domain of the $\alpha$ subunit of FAS, given the fit-to-density of
197    an ACP domain homology model. This additional density was largely missing in the
198    original map. Ultimately, the new density was of sufficient quality to build an atomic

199    model of the ACP domain (Fig 2E). Interestingly, ACP domain residue S178 (which

200    tethers the growing fatty acid chain) is located ~18 Å away from the KS active site,

201    which is in agreement with the length of the PPT arm (18 Å)[27]. Some classes contained

202    additional low-resolution density at the edge of the masked region used for focussed

203    classification (Supplementary Fig S2A). To examine whether this corresponded to

204    ACP domains positioned differently within the complex interior that were not fully

205    contained within the masked region, focussed classification was repeated with an

206    expanded mask (Supplementary Fig S2B). In addition to a class containing well-

207    resolved ACP density, multiple classes containing low-resolution ACP-sized density in

208    different positions were observed (Fig 2F). However, these classes comprised

209    relatively few subparticles and asymmetric reconstruction only resulted in poor

210    resolution (~8 Å).

211

212    Focussed classification was also performed in an attempt to resolve the PPT domain.

213    While a low-resolution class was identified as containing PPT density (Supplementary

214    Fig S3), further reconstruction did not yield density sufficient for model building.

215

216    Interestingly, we observed additional density on the exterior of the FAS complex, not

217    accounted for by the atomic model (Fig 2G). This density is weaker than for the rest

218    of the complex and is not well resolved, indicating that the component is flexible and/or

219    that there is not full occupancy. The additional, external density appears to extend

220    outwards from V534 ($\alpha$ subunit). While residues 535-598 are not resolved, the density

221    remains localised close to V534 and does not provide a logical connecting trace to

222    A599. The extra density was also present in a 4.3-Å resolution reconstruction

223    determined from the same data but without the imposition of symmetry, suggesting

224    that this is not simply an artefact of symmetry averaging. However, given the poor

225    resolution of this region of the map, we were unable to determine its identity.

226

227    **Distinct structural features of *P. pastoris* FAS**

228    To identify unique structural features of *P. pastoris* FAS, we carried out a comparative

229    structural analysis. While PDBeFold[28] suggested that the closest structural matches

230    to *P. pastoris* FAS were cryoEM structures of *C. albicans* FAS (PDB 6U5W, PDB

231    6U5V)[18], we chose to compare our structure with *S. cerevisiae* FAS, a better

232   characterised FAS with greater relevance to metabolic engineering attempts. At the
233   peptide sequence level, *P. pastoris* FAS α and β subunits show 69% and 63% identity
234   with their equivalents in *S. cerevisiae*. We compared our structure with a recently
235   published 3.1-Å resolution structure of FAS from *S. cerevisiae* (PDB 6TA1)[17]. After
236   aligning the two structures, a root mean-square deviation (RMSD) value between
237   equivalent Cα atom pairs was calculated as 7.1 Å, indicating a notable level of
238   difference between the two models (Fig 3A). However, aligning the models by
239   individual subunits gave RMSD values of 1.7 Å (α-α), and 2.2 Å (β-β), suggesting that
240   this may be partially attributable to differences in the spatial relationship between the
241   α and β subunits in each model. Visual inspection confirmed that several domains
242   appeared shifted, particularly the MPT domain.

243

244   Closer examination revealed many differences in the path traced by the peptide
245   backbone. One instance of this is a loop in the MPT domain, which is shifted by 16 Å
246   at its turning point (D1761) (Fig 3B). Interestingly, when displaying density at a low
247   threshold so that even weak density is visible (0.5 σ), we also saw density tracing the
248   alternative loop conformation seen in the *S. cerevisiae* yeast structure. Other loops
249   and linker regions throughout the β subunit also showed obvious differences in
250   conformation, including in the DH domain (F1283-V1289, E1505-I1511), MPT domain
251   (A1859-Y1870), and structural domains/linker regions (G75-N78, A914-G919) (Fig
252   3C). Furthermore, a small sequence insertion of three amino acids introduced a kink
253   into the outer strand of a β-sheet within the DH domain (A1553-L1558) (Fig 3D). Of
254   particular interest is a sequence of residues (F1113-T1135) linking the ER domain to
255   the DH-adjacent structural domain, which was mostly unmodeled in the *S. cerevisiae*
256   FAS structure (Fig 3E). For the structure reported here, this linker region was well-
257   resolved and differed significantly from the terminal parts of the linker that are resolved
258   in PDB 6TA1.

259

260   There are also subtle rotameric differences in some of the enzymatic domain active
261   sites. In particular, Q171 was shifted within the active site of the AT domain (Fig 3F).
262   H749 of the ER domain was also pointing in the opposite direction to the equivalent
263   histidine in *S. cerevisiae* FAS (Fig 3G).

264

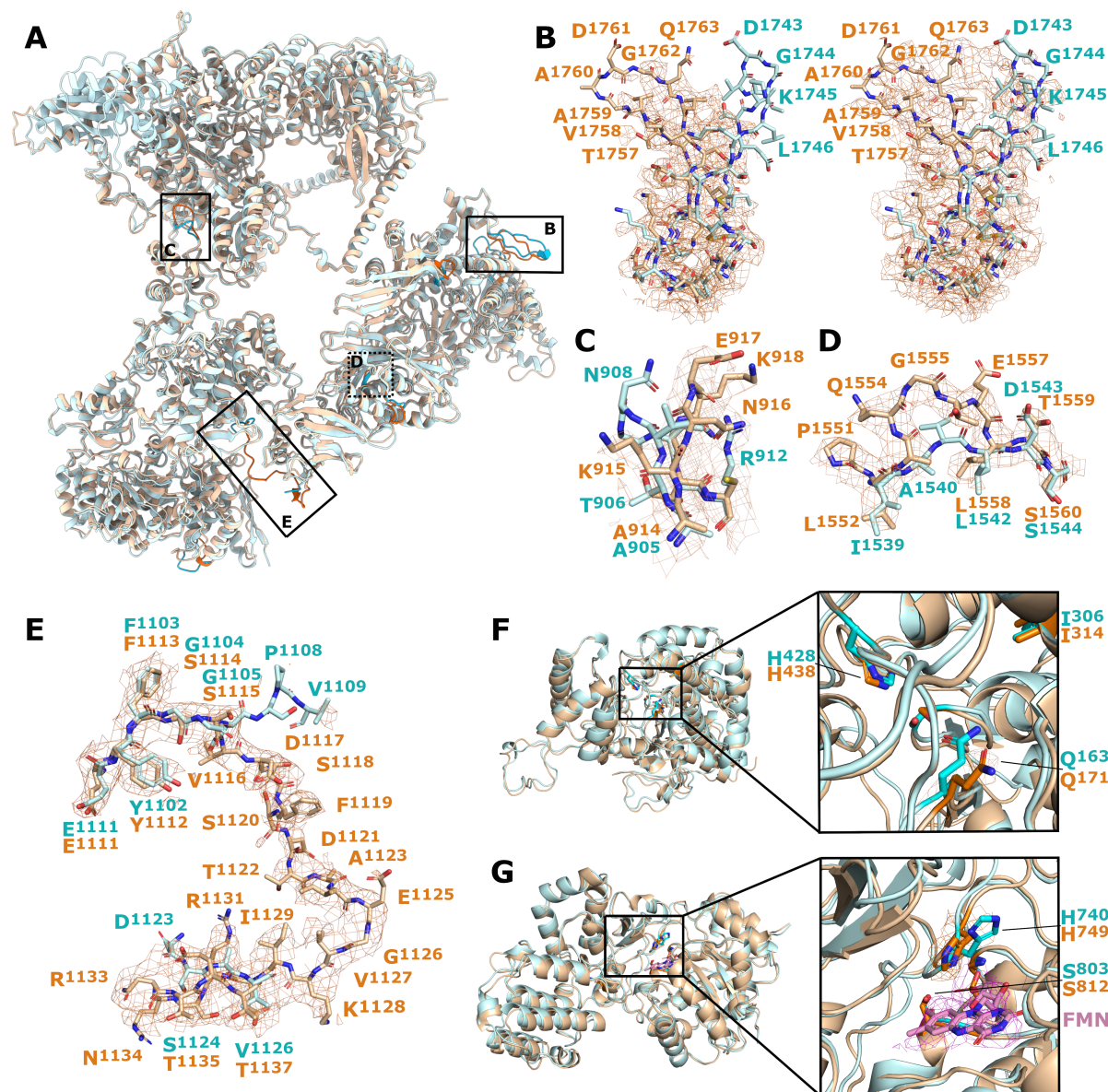*Figure 3. Unique structural features of P. pastoris FAS. (A) Overlay of P. pastoris FAS (orange) and S. cerevisiae FAS (PDB 6TA1, blue) from Joppe et al. (2020)[17], with differences highlighted by stronger colours. Enlarged images are indicated on the map with boxes. (B) Loop region comprising residues 1753-1768, highlighting the different positioning compared to the equivalent region from S. cerevisiae FAS. The P. pastoris density map is overlaid at high contour level (left) and low contour level (right). (C-E) Other regions from different parts of the protein are highlighted and compared with equivalent regions of S. cerevisiae FAS, including the loop comprising residues 914-919 (C), the beta strand comprising residues 1553-1558 (D) and the additional resolved linking region comprising residues 1113-1135 (E). (F) The AT domain, with enlarged image highlighting different positioning of the active site residue Q171. (G)*

11

277 *The ER domain, with enlarged image highlighting different positioning of the active*

278 *site residue H749. FMN and its corresponding density are shown in pink.*

279

## Discussion

281 We serendipitously identified fatty acid synthase, which is constitutively expressed in

282 yeast[29], as a contaminant in a cryoEM data set of a hepatitis B core VLP preparation

283 purified from *P. pastoris*. Subsequent analysis of raw micrographs revealed that FAS

284 was readily separated from the VLPs. As such, we think it unlikely that FAS co-purified

285 as a result of a specific interaction with the VLPs. Rather, its presence in the VLP

286 preparation was probably as a result of its mass being sufficiently similar to co-purify

287 on sucrose density gradients (FAS 2.6 MDa; *T*=3 VLP 4.7 MDa; *T*=4 VLP 6.3 MDa).

288 By processing this 'contaminant' data and using focussed 3D classification

289 techniques, we were able to determine the structure of the *P. pastoris* FAS to 3.1 Å

290 resolution, and build an atomic model for the complex, including a model for the mobile

291 ACP domain.

292

293 Interestingly, we did not observe signs of partial denaturation of FAS in 2D class

294 averages, as was seen previously for a different yeast FAS structure[16]. It is possible

295 that the presence of VLPs in the sample affected the ice thickness or crowded the air-

296 water interface (which is known to induce denaturation[16]), reducing any interactions

297 between the interface and FAS. However, we suspect that the lack of partial

298 denaturation is more likely a result of the continuous thin carbon film used for making

299 these cryoEM grids, which may trap FAS particles away from the air-water interface.

300 While the presence of a thin carbon film adds a background that reduces the signal-

301 to-noise ratio of particles (and can therefore limit the resolution), we were able to

302 resolve our map to 3.1 Å, equivalent to that of the structure reported by Joppe *et al.*

303 (2020)[17] and sufficient to build a molecular model for FAS. Therefore, using a

304 continuous thin carbon film may be a simple alternative to coating grids with

305 hydrophilized graphene, when the size of the target protein (and hence its signal

306 strength) is similar to FAS.

307

308 The overall structure was typical of a yeast FAS. As has previously been observed for

309 yeast FAS structures, the PPT domain was missing[16] and the quality of the ACP

310 domain density was relatively poor. In this case, density corresponding to the ACP

12

311 domain was initially of insufficient quality for molecular modelling, but this was resolved
312 by focussed classification. Given the known mobile nature of the ACP domain[13], this
313 was unsurprising. Focussed classification led to an improvement in the strength and
314 quality of the ACP density that was sufficient to allow atomic modelling, probably as
315 result of grouping together only subparticles with ACP domains in the same relative
316 position (adjacent to the KS domain, as has been observed in several other yeast FAS
317 structures[17,27]) at the time of vitrification. Use of an expanded mask for focussed
318 classification revealed classes with putative ACP density in other positions within the
319 complex interior. These classes contained relatively few subparticles, suggesting that
320 the vast majority of ACP domains were adjacent to the KS domain, with the remainder
321 either missing or occupying other positions. The lack of PPT domain density is likely
322 to be a result of loss of this domain from most complexes during sample
323 purification/preparation, as has previously been noted[16,17]. Since our initial aim was to
324 purify VLPs, not FAS, no special care was taken to ensure the complex was kept intact
325 (although the ER domain cofactor FMN was clearly present in the density map,
326 providing evidence that the complex was still likely to have been active). While
327 focussed classification was not sufficient to resolve the PPT domain, one class did
328 show weak density corresponding to the PPT domain, suggesting that it was retained
329 in at least some particles.

331 We identified a number of structural differences between the *P. pastoris* FAS structure
332 reported here and a recent 3.1-Å resolution structure from *S. cerevisiae* (PDB 6TA1)[17],
333 another member of the yeast family *Saccharomycetaceae*. The MPT domain was
334 distinctly shifted relative to its position in *S. cerevisiae* FAS. This is of particular
335 importance, because this domain is the target of one approach to engineer FAS
336 complexes to produce short chain fatty acids[4]. Many intradomain differences affected
337 structural (non-enzymatic) components of the complex, including a loop within the
338 MPT domain from S1752 – K1768. This loop was particularly interesting, as very weak
339 density tracing the backbone of the alternative (*S. cerevisiae*) conformation also
340 became visible at low contour thresholds. This is indicative of a mixed population of
341 conformations in *P. pastoris* FAS, with most complexes sampling the conformation
342 modelled, and a smaller subpopulation sampling the conformation seen for *S.*
343 *cerevisiae* FAS. This loop may plausibly be dynamic, an idea reinforced by the local

13

344  resolution of the loop being poorer than average, at around 3.7 – 4.1 Å resolution
345  (Supplementary Fig S1).

346

347  We also identified differences in the active sites of two enzymatic domains. In the AT
348  domain, Q171 forms part of a tight hydrogen bond network around the active serine
349  (S282) and its backbone amide also contributes to an oxyanion hole, which plays a
350  role in promoting the transfer of malonyl to the thiol group of the ACP[6,12]. While the
351  alternative rotamer observed here is unlikely to affect the oxyanion hole, the structure
352  suggests a subtle alteration in the arrangement/spacing of the hydrogen bond network
353  at the catalytic centre of the AT domain. Aside from Q171, the catalytic histidine of the
354  ER domain (H749) was seen to be in a 'flipped' conformation relative to its equivalent
355  in *S. cerevisiae* FAS[12,17]. Interestingly, the conformation reported here is much closer
356  to that seen in a crystal structure of *S. pneumoniae* FabK in its active state (PDB 2Z6I),
357  a homologous enzyme that forms part of its type II FAS system[30]. Whether these
358  changes to active site residues have functional significance is unclear. However, it
359  should be noted that the *S. cerevisiae* FAS was incubated with NADPH and malonyl-
360  CoA prior to vitrification in order to drive FA synthesis to completion[17]. The *P. pastoris*
361  FAS reported here received no such treatment and as such, reaction status was likely
362  less uniform and potentially incomplete.

363

364  In conclusion, despite non-optimised sample preparation and using just ~37,000
365  particles, we were able to determine the structure of *P. pastoris* FAS to 3.1-Å
366  resolution and identify structural differences with a related yeast FAS. As well as
367  highlighting the importance of considering 'contaminant data' in cryoEM data sets, the
368  structure reported here could prove a useful resource for future efforts to engineer
369  yeast FAS.

370

371  **<u>Methods</u>**

372  **Cells**
373  FAS was purified from PichiaPink™ yeast strain one (Invitrogen, USA), which was
374  grown according to the manufacturer's instructions.

375

14

**Yeast transformation and induction**

While the focus of this work was FAS, which is constitutively expressed in yeast[29], our initial aim was to use yeast to express and purify VLPs composed of hepatitis B virus tandem core proteins[24] with a SUMO-binding affimer[25] inserted into the major immunodominant region (MIR) (construct available upon request) for structural characterisation. As such, VLP expression was induced in the transformed yeast prior to purification, as described previously[31]. Briefly, glycerol stocks known to exhibit good levels of expression were cultured in yeast extract-peptone-dextrose (YPD), supplemented with 50 µg/mL ampicillin, at 28°C, 250 rpm for 48 h. 2 ml of the high-density starter culture was then transferred to 200 mL YPD and incubated for another 24 h under the same conditions. To induce expression of VLPs, cells were pelleted ($1500 \times g$, 20 min) and resuspended in 200 mL yeast extract-peptone-methanol (YPM; 0.5% [v/v] methanol) for a further 48-hour incubation, with methanol added to a final concentration of 0.5% (v/v) 24 h post-induction. Cells were subsequently collected by pelleting at $2000 \times g$ (20 min), resuspended in 30 mL breaking buffer (50 mM sodium phosphate, 1 mM phenylmethylsulfonyl fluoride [PMSF], 1 mM EDTA, 5% glycerol, pH 7.4) and stored at -20°C prior to purification.

**Co-purification of FAS with VLPs**

Though our aim was to purify VLPs (as described previously[31]) for structural characterisation, FAS co-purified with the particles. Frozen *P. pastoris* stocks that had been induced to express VLPs were thawed and incubated with 0.1% (v/v) Triton-X100 for 30 min. Cells were lysed using a CF-1 cell disruptor at ~275 MPa and cooled to 4°C, before the lysate was centrifuged first at 4000 rpm (30 min, 4°C), then at 10,000 $\times g$ (30 min, 4°C) to remove insoluble material. The supernatant was supplemented with 2 mM MgCl and treated with HS-nuclease (2BScientific) for 1.5 h at room temperature, then mixed with saturated ammonium sulphate solution (40% [v/v]) and incubated overnight at 4°C for precipitation. Precipitated protein was recovered by pelleting at 4000 rpm (30 min, 4°C) and solubilised by resuspending in PBS (supplemented with 0.1% [v/v] Triton-X100). After further centrifugation at 4000 rpm (30 min, 4°C), then 10,000 $\times g$ (30 min, 4°C) to remove any remaining insoluble material, the supernatant was pelleted through a 30% sucrose cushion (w/v) at 151,000 $\times g$ (3.5 h, 4°C, SW-32 Ti). The pellet was resuspended in PBS

15

409  (supplemented with 1% [v/v] NP-40 and 0.5% [w/v] sodium deoxycholate), then

410  clarified at 10,000 × *g* (10 min, 4°C) before loading onto a 15-45% (w/v) sucrose

411  gradient for ultracentrifugation at 151,000 × *g* (3 h, 4°C). 2 ml fractions were collected

412  and those containing VLPs were identified by western blot. A centrifugal filter (100K,

413  5 mL, Pall Life Sciences) was used according to the manufacturer's instructions to

414  remove sucrose and concentrate the peak fraction to 0.5 mL.

415

**Electron microscopy**

417  CryoEM grids were prepared by applying 3 µL of a VLP preparation with contaminating

418  FAS complex in PBS to lacey carbon 400-mesh copper grids coated with a <3-nm

419  continuous carbon film (Agar Scientific, Stansted, UK), after glow-discharging the grids

420  in air (10 mA, 30 seconds) using a PELCO easiGlow™ Glow Discharge System (Ted

421  Pella). Following application of sample, grids were incubated at 8°C, 80% relative

422  humidity for 30 seconds, then blotted to remove excess liquid and vitrified in liquid

423  nitrogen-cooled liquid ethane using a LEICA EM GP plunge freezing device (Leica

424  Microsystems, Wetzlar, Germany). Blotting time parameters were varied to increase

425  the likelihood of recovering a grid with optimal ice thickness. Following plunge freezing,

426  grids were stored in liquid nitrogen. Grids were imaged using an FEI Titan Krios

427  transmission electron microscope (ABSL, University of Leeds, Leeds, UK) operating

428  at 300 kV. A magnification of 75,000× was used for a calibrated object sampling of

429  1.065 Å/pixel. Detailed information on data collection parameters is provided in Table

430  S1.

431

**Image processing**

433  The RELION 3.0 pipeline[32] was used for image processing. Raw micrographs were

434  first motion corrected using MotionCor2[33], then CTF parameters were estimated using

435  Gctf[34]. Particles were selected from a subset of micrographs by manual picking and

436  were then differentiated by 2D classification. High quality 2D classes were used as

437  templates for autopicking the complete data set. A low picking threshold was specified

438  to autopicking to minimize the number of 'missed' VLPs. Picked particles were 2×

439  down-sampled, then subject to 2D classification (with CTFs ignored until the first

440  peak), leading to the identification of FAS-containing classes. 2D classes containing

441  FAS were taken forward for initial model generation and used as templates for FAS-

442   specific autopicking. Autopicked FAS particles were extracted without down-sampling

443   and subjected to two rounds of 2D classification (first with CTFs ignored until the first

444   peak, then without). Particles in high quality classes were taken forward for 3D

445   refinement (with D3 symmetry applied) with subsequent masking and sharpening.

446   Following this, several cycles of CTF refinement (with per-particle astigmatism

447   correction and beamtilt estimation), Bayesian polishing and 3D refinement (with

448   masking and use of solvent-flattened FSCs) were performed to improve the resolution

449   of the map. After sharpening, the resolution of the final map was determined using the

450   'gold standard' Fourier shell correlation criterion (FSC = 0.143) (Table S1, Figure S1).

451   RELION was used to estimate local resolution and generate a local resolution-filtered

452   map.

453

454   To resolve the flexible ACP, focussed 3D classification was performed as described

455   previously[35–37]. Briefly, a cylindrical mask was generated in SPIDER[38] and resampled

456   onto the D3-symmetric density map of FAS, such that it was positioned over the weak

457   ACP density. The relion_symmetry_expand tool was used to assign 6 symmetrically

458   redundant orientations to each particle contributing to a symmetric reconstruction,

459   such that the ACP domain in each symmetry-related position would be included in the

460   classification. These symmetry-expanded particles were then subject to masked 3D

461   classification without re-alignment using a regularisation parameter ("T" number) of

462   40. Particles contributing to the ACP density-containing class were taken forward for

463   asymmetric reconstruction using the relion_reconstruct tool.

464

**Model building and refinement**

466   To generate a preliminary model for the asymmetric unit of FAS, the peptide

467   sequences of *P. pastoris* FAS $\alpha$ (NCBI: XP_002490414.1) and $\beta$ (NCBI:

468   XP_002489642.1) subunits were used to generate a homology model using the

469   SWISS-MODEL web server[26]. The homology model was rigid-body fitted into the

470   sharpened FAS density map using UCSF Chimera[39], then refined in Coot[40]. The

471   refined model was symmetrised in UCSF Chimera, then subject to real space

472   refinement in Phenix[41] to improve simultaneously the fit of the model to the density

473   map and model geometry. Several iterations between refinement in Coot and

474   refinement in Phenix were performed before validating the model with Molprobity[42].

17

475

**Visualization and structure comparison**

477 Density map and atomic model visualization was performed and figures were

478 generated using UCSF Chimera[39] and UCSF Chimera X[43]. Structural alignment and

479 RMSD calculations were performed using the 'MatchMaker' tool with default settings

480 in UCSF Chimera. PDBeFold (the protein structure comparison service at EBI

481 [http://www.ebi.ac.uk/msd-srv/ssm])[28] was used to probe structural similarity between

482 the FAS structure reported here and other molecular structures within the PDB.

483 Particle orientation distribution was visualized using an adapted version[44] of a script

484 from Naydenova & Russo (2017)[45].

485

**Quantification and statistical analysis**

487 Where appropriate, statistical details are given in the Method Details section. Table

488 S1 contains quantitative parameters related to data collection and image processing.

489 Table S2 contains validation statistics related to model building.

490


491 <u>**Data Availability Statement**</u>

492 The *P. pastoris* FAS cryoEM map was deposited in the Electron Microscopy Data Bank

493 (EMD-12138) along with the reconstructed ACP domain-containing map from

494 focussed classification (EMD-12139). The atomic coordinates for the FAS asymmetric

495 unit (PDB-7BC4) and the ACP domain (PDB-7BC5) were deposited in the Protein Data

496 Bank.

497

498 <u>**References**</u>

499

500 1.    Tehlivets, O., Scheuringer, K. & Kohlwein, S. D. Fatty acid synthesis and elongation in
501       yeast. *Biochim. Biophys. Acta.* **1771**, 255–270 (2007).

502 2.    Heil, C. S., Wehrheim, S. S., Paithankar, K. S. & Grininger, M. Fatty acid biosynthesis:
503       chain-length regulation and control. *ChemBioChem* **20**, 2298–2321 (2019).

504 3.    Gajewski, J. *et al.* Engineering fatty acid synthases for directed polyketide production.
505       *Nat. Chem. Biol.* **13**, 363–365 (2017).

506 4.    Gajewski, J., Pavlovic, R., Fischer, M., Boles, E. & Grininger, M. Engineering fungal
507       de novo fatty acid synthesis for short chain fatty acid production. *Nat. Commun.* **8**,
508       14650 (2017).

5.    Beld, J., Lee, D. J. & Burkart, M. D. Fatty acid biosynthesis revisited: structure elucidation and metabolic engineering. *Mol. BioSyst.* **11**, 38–59 (2015).

6.    White, S. W., Zheng, J., Zhang, Y. M. & Rock, C. O. The structural biology of type II fatty acid biosynthesis. *Annu. Rev. Biochem.* **74**, 791–831 (2005).

7.    Maier, T., Leibundgut, M., Boehringer, D. & Ban, N. Structure and function of eukaryotic fatty acid synthases. *Q. Rev. Biophys.* **43**, 373–422 (2010).

8.    Schweizer, E. & Hofmann, J. Microbial type I fatty acid synthases (FAS): major players in a network of cellular FAS systems. *Microbiol. Mol. Biol. Rev.* **68**, 501–517 (2004).

9.    Stoops, J. K., Kolodziej, S. J., Schroeter, J. P., Bretaudiere, J. P. & Wakil, S. J. Structure-function relationships of the yeast fatty acid synthase: negative-stain, cryo-electron microscopy, and image analysis studies of the end views of the structure. *Proc. Natl. Acad. Sci. USA* **89**, 6585–6589 (1992).

10.   Jenni, S., Leibundgut, M., Maier, T. & Ban, N. Architecture of a fungal fatty acid synthase at 5 Å resolution. *Science* **311**, 1263–1267 (2006).

11.   Jenni, S. *et al.* Structure of fungal fatty acid synthase and implications for iterative substrate shuttling. *Science* **316**, 254–261 (2007).

12.   Lomakin, I. B., Xiong, Y. & Steitz, T. A. The crystal structure of yeast fatty acid synthase, a cellular machine with eight active sites working together. *Cell* **129**, 319–332 (2007).

13.   Gipson, P. *et al.* Direct structural insight into the substrate-shuttling mechanism of yeast fatty acid synthase by electron cryomicroscopy. *Proc. Natl. Acad. Sci. USA* **107**, 9164–9169 (2010).

14.   Crosby, J. & Crump, M. P. The structural role of the carrier protein - active controller or passive carrier. *Nat. Prod. Rep.* **29**, 1111–1137 (2012).

15.   Fichtlscherer, F., Wellein, C., Mittag, M. & Schweizer, E. A novel function of yeast fatty acid synthase. Subunit α is capable of self-pantetheinylation. *Eur. J. Biochem.* **267**, 2666–2671 (2000).

16.   D'Imprima, E. *et al.* Protein denaturation at the air-water interface and how to prevent it. *eLife* **8**, e42747 (2019).

17.   Joppe, M. *et al.* The resolution revolution in cryoEM requires high-quality sample preparation: a rapid pipeline to a high-resolution map of yeast fatty acid synthase. *IUCrJ* **7**, 220–227 (2020).

18.   Lou, J. W., Iyer, K. R., Hasan, S. M. N., Cowen, L. E. & Mazhab-Jafari, M. T. Electron cryomicroscopy observation of acyl carrier protein translocation in type I fungal fatty acid synthase. *Sci. Rep.* **9**, 12987 (2019).

19.   Singh, K. *et al.* Discovery of a regulatory subunit of the yeast fatty acid synthase. *Cell* **180**, 1130-1143.e20 (2020).

20.   Ahmad, M., Hirz, M., Pichler, H. & Schwab, H. Protein expression in Pichia pastoris: recent achievements and perspectives for heterologous protein production. *Appl.*

549          *Microbiol. Biotechnol.* **98**, 5301–5317 (2014).

550   21.   Yang, Z. & Zhang, Z. Engineering strategies for enhanced production of protein and
551          bio-products in Pichia pastoris: A review. *Biotechnol. Adv.* **36**, 182–195 (2018).

552   22.   Cereghino, J. L. & Cregg, J. M.  Heterologous protein expression in the
553          methylotrophic yeast Pichia pastoris . *FEMS Microbiol. Rev.* **24**, 45–66 (2000).

554   23.   Meesapyodsuk, D., Chen, Y., Ng, S. H., Chen, J. & Qiu, X. Metabolic engineering of
555          Pichia pastoris to produce ricinoleic acid, a hydroxy fatty acid of industrial importance.
556          *J. Lipid Res.* **56**, 2102–2109 (2015).

557   24.   Peyret, H. *et al.* Tandem Fusion of hepatitis B core antigen allows assembly of virus-
558          like particles in bacteria and plants with enhanced capacity to accommodate foreign
559          proteins. *PLoS One* **10**, e0120751 (2015).

560   25.   Tiede, C. *et al.* Affimer proteins are versatile and renewable affinity reagents. *eLife* **6**,
561          e24903 (2017).

562   26.   Waterhouse, A. *et al.* SWISS-MODEL: Homology modelling of protein structures and
563          complexes. *Nucleic Acids Res.* **46**, W296–W303 (2018).

564   27.   Leibundgut, M., Jenni, S., Frick, C. & Ban, N. Structural basis for substrate delivery by
565          acyl carrier protein in the yeast fatty acid synthase. *Science* **316**, 288–290 (2007).

566   28.   Krissinel, E. & Henrick, K. Secondary-structure matching (SSM), a new tool for fast
567          protein structure alignment in three dimensions. *Acta Crystallogr. D Biol. Crystallogr.*
568          **60**, 2256–2268 (2004).

569   29.   Schüller, H. J., Schütz, A., Knab, S., Hoffmann, B. & Schweizer, E. Importance of
570          general regulatory factors Rap1p, Abf1p and Reb1p for the activation of yeast fatty
571          acid synthase genes FAS1 and FAS2. *Eur. J. Biochem.* **225**, 213–222 (1994).

572   30.   Saito, J. *et al.*  Crystal structure of enoyl-acyl carrier protein reductase (FabK) from
573          Streptococcus pneumoniae reveals the binding mode of an inhibitor . *Protein Sci.* **17**,
574          691–699 (2008).

575   31.   Sherry, L. *et al.*  Comparative molecular biology approaches for the production of
576          poliovirus virus-like particles using Pichia pastoris. *mSphere* **5**, e00838-19 (2020).

577   32.   Zivanov, J. *et al.* New tools for automated high-resolution cryo-EM structure
578          determination in RELION-3. *eLife* **7**, e42166 (2018).

579   33.   Zheng, S. Q. *et al.* MotionCor2: anisotropic correction of beam-induced motion for
580          improved cryo-electron microscopy. *Nat. Methods* **14**, 331–332 (2017).

581   34.   Zhang, K. Gctf: real-time CTF determination and correction. *J. Struct. Biol.* **193**, 1–12
582          (2016).

583   35.   Scheres, S. H. W. Processing of structurally heterogeneous cryo-EM data in RELION.
584          *Methods Enzymol.* **579**, 125–157 (2016).

585   36.   Conley, M. J. *et al.* Calicivirus VP2 forms a portal-like assembly following receptor
586          engagement. *Nature* **565**, 377–381 (2019).

587    37.    Snowden, J. S. *et al.* Dynamics in the murine norovirus capsid revealed by high-
588            resolution cryo-EM. *PLoS Biol.* **18**, e3000649 (2020).

589    38.    Frank, J. *et al.* SPIDER and WEB: processing and visualization of images in 3D
590            electron microscopy and related fields. *J. Struct. Biol.* **116**, 190–199 (1996).

591    39.    Pettersen, E. F. *et al.* UCSF Chimera - a visualization system for exploratory research
592            and analysis. *J. Comput. Chem.* **25**, 1605–1612 (2004).

593    40.    Emsley, P., Lohkamp, B., Scott, W. G. & Cowtan, K. Features and development of
594            Coot. *Acta Crystallogr. D Biol. Crystallogr.* **66**, 486–501 (2010).

595    41.    Adams, P. D. *et al.* PHENIX: a comprehensive Python-based system for
596            macromolecular structure solution. *Acta Crystallogr. D Biol. Crystallogr.* **66**, 213–221
597            (2010).

598    42.    Chen, V. B. *et al.* MolProbity: all-atom structure validation for macromolecular
599            crystallography. *Acta Crystallogr. D. Biol. Crystallogr.* **66**, 12–21 (2010).

600    43.    Goddard, T. D. *et al.* UCSF ChimeraX: meeting modern challenges in visualization
601            and analysis. *Protein Sci.* **27**, 14–25 (2018).

602    44.    Klebl, D. P. *et al.* Need for speed: examining protein behavior during cryoEM grid
603            preparation at different timescales. *Structure* **28**, 1238–1248.e4 (2020).

604    45.    Naydenova, K. & Russo, C. J. Measuring the effects of particle orientation to improve
605            the efficiency of electron cryomicroscopy. *Nat. Commun.* **8**, 629 (2017).

606
## 607    Acknowledgments

617

## 618    Author Contributions

619    JA and LS maintained *P. pastoris*; JA purified FAS; JSS prepared samples for cryoEM,

620    carried out cryoEM data collection and performed image processing; JSS, JA, DJR,

621 NAR and NJS analysed data; JSS, NAR and NJS wrote the paper; LS, MS, DJR, NAR

622 and NJS provided supervision.

623

624 **Additional Information**

625 The authors declare no competing interests.

626